photonics

MDPI

Article

Tunable Multicriticality in a Dissipative Superradiant Phase Transition via Optical Squeezing

Yuanyi Huang, Gui-Lei Zhu *, Lin Cheng and Xiaoguang Wang *

Zhejiang Key Laboratory of Quantum State Control and Optical Field Manipulation, Department of Physics, Zhejiang Sci-Tech University, Hangzhou 310018, China; 2023326690020@mails.zstu.edu.cn (Y.H.); chenglin@zstu.edu.cn (L.C.)

* Correspondence: guileizhu@zstu.edu.cn (G.-L.Z.); xgwang@zstu.edu.cn (X.W.)

Abstract

Dissipation can fundamentally reconstruct the multicritical structure of driven-dissipative light–matter systems. In the interpolating Dicke–Tavis–Cummings model, cavity loss eliminates the $U(1)$-symmetric superradiant phase on the Tavis–Cummings line $\lambda_x = \lambda_y$ and splits the original multicritical point into a pair of dissipation-induced tricritical points. Here, we show that intracavity optical squeezing provides a coherent means of continuously reshaping this loss-generated multicritical structure. The single-mode parametric interaction acts asymmetrically on the two cavity quadratures, thereby deforming the phase boundaries and continuously tuning the dissipation-induced tricritical points. We analytically determine the phase boundaries and the evolution of the tricritical structure with the parametric gain and cavity dissipation, and show that the two tricritical points coalesce in the weak-loss limit. Photon-number fluctuations provide clear quantum signatures of the squeezing-controlled multicritical structure.

Keywords: superradiant phase transition; multicriticality; optical squeezing; driven-dissipative systems; Dicke model

1. Introduction

Understanding quantum phase transitions and criticality is a central topic in modern condensed matter physics and quantum optics [1,2]. A paradigmatic example is the superradiant phase transition in Dicke-type models, where an ensemble of two-level systems collectively interacts with a single bosonic cavity mode [3,4]. When the atom–field coupling strength exceeds a critical value λ_c, the system undergoes a transition from the normal phase to a superradiant phase [5–14]. Beyond conventional critical points, multicritical structures have attracted considerable attention. Of particular interest are tricritical points (TCPs) [15–18] where the first- and second-order phase transition boundaries meet. In addition to their fundamental importance in nonequilibrium many-body physics, multicritical regimes are expected to enhance the response of a system to external perturbations [19] and therefore offer potential applications in quantum sensing and metrology [20–26].

A paradigmatic model exhibiting such multicritical behavior is the interpolating Dicke–Tavis–Cummings (IDTC) model [27]. In this model, the two quadratures of a single cavity field couple independently to two orthogonal components of a collective spin, with coupling strengths λ_x and λ_y. A key feature of the IDTC model is the emergence of a continuous $U(1)$ symmetry along the Tavis–Cummings line ($\lambda_x = \lambda_y$), where the normal phase and two superradiant phases meet at a tricritical point.

Check for updates

Received: 18 August 2026
Revised: 8 September 2026
Accepted: 14 September 2026
Published: 18 September 2026

Copyright: © 2026 by the authors. Licensee MDPI, Basel, Switzerland. This article is an open access article distributed under the terms and conditions of the Creative Commons Attribution (CC BY) license.

Realistic light–matter systems are inevitably coupled to their environment. Remarkably, even infinitesimal cavity dissipation fundamentally reconstructs the phase diagram [28–32], destroying the $U(1)$-symmetric superradiant phase on the Tavis–Cummings line and opening a normal-phase sliver between the two Dicke-like superradiant phases [33]. Consequently, the original multicritical point splits into two nonequilibrium tricritical points. However, once the system is fixed, the cavity decay rate is generally difficult to tune by external fields.

Optical squeezing and parametric driving have been explored as effective means of controlling critical phenomena in light–matter systems. In particular, intracavity squeezing has been shown to induce symmetry-breaking superradiant transitions in Tavis–Cummings-type systems [34], and squeezed-light-induced phase transitions have also been studied in the Jaynes–Cummings model [35,36]. More recently, squeezing-assisted multicritical phenomena have been explored in other cavity-QED configurations [37,38]. In contrast to these studies, which focus on squeezing-induced superradiant transitions or tricriticality, the present work addresses the coherent control of a tricritical pair generated by cavity dissipation.

In this work, we introduce intracavity optical parametric amplification into the dissipative IDTC model to achieve coherent control of the dissipation-induced multicritical structure. A classically pumped $\chi^{(2)}$ nonlinear medium generates a coherent two-photon term of the form $G(a^2 + a^{\dagger 2})$, where the parametric gain G is controlled by the external pump amplitude [39–42]. The squeezing interaction reduces the continuous $U(1)$ symmetry on the Tavis–Cummings line to the discrete Z_2 symmetry, allowing superradiant solutions to reappear on this line, consistent with the squeezing-induced symmetry-breaking mechanism reported previously [34]. The coherent interaction continuously changes the superradiant phase boundaries and displaces the two dissipation-induced tricritical points in the (λ_x, λ_y) plane. We derive the first- and second-order phase boundaries and obtain explicit expressions for the locations of both tricritical points as functions of G and κ. We further show that finite squeezing breaks the $\lambda_x \leftrightarrow \lambda_y$ exchange symmetry and asymmetrically deforms the tricritical pair, whereas the two points coalesce in the weak-loss limit. We further characterize their evolution through photon-number fluctuations.

The remainder of this paper is organized as follows. In Section 2, we introduce the dissipative interpolating Dicke–Tavis–Cummings model with intracavity optical parametric amplification, discuss its symmetry properties, and formulate the corresponding open-system dynamics. In Section 3, we derive the semiclassical steady-state solutions and the analytical phase boundaries, and characterize the resulting superradiant phase diagram. In Section 4, we focus on the tunable tricritical structure, derive the locations of the two tricritical points, and analyze their evolution under variation of the parametric gain and cavity dissipation. In Section 5, we investigate quantum fluctuations around the stable mean-field steady states and identify their signatures near the critical boundaries. Finally, Section 6 summarizes our main results and conclusions.

2. Model

We consider an ensemble of N identical two-level atoms, each coupled to both quadratures of a bosonic mode (e.g., the electric and magnetic field components of an electromagnetic field) that contains a second-order $\chi^{(2)}$ nonlinear crystal. Such two-quadrature light–matter couplings can, in principle, be engineered in circuit-QED architectures, where artificial atoms couple capacitively and inductively to a resonator, or through cavity-assisted Raman interaction channels [10,27]. The nonlinear medium is driven by a strong classical pump field with frequency ω_p, giving rise to intracavity optical parametric amplification

(OPA) [34,37,38,41,42]. Setting $\hbar = 1$, the effective Hamiltonian in the rotating frame at half the pump frequency, $\omega_p/2$, is

$$H_{\text{eff}} = \Delta_c a^\dagger a + \Delta_q S_z + \frac{2\lambda_x}{\sqrt{N}} S_x (a + a^\dagger) + i\frac{2\lambda_y}{\sqrt{N}} S_y (a - a^\dagger) + G(a^2 + a^{\dagger 2}), \tag{1}$$

where a ($a^\dagger$) denotes the annihilation (creation) operator of the cavity mode, and $S_\mu = \frac{1}{2}\sum_{j=1}^{N} \sigma_\mu^{(j)}$ ($\mu = x, y, z$) are the collective spin operators, with $\sigma_\mu^{(j)}$ the Pauli matrices for the jth atom. The parameters λ_x and λ_y characterize the anisotropic light–matter couplings. The effective parametric gain is given by $G = \chi^{(2)}|\beta'|$, where β' is the coherent pump amplitude and $\chi^{(2)}$ denotes the effective three-wave-mixing strength. The effective parametric gain G can be continuously controlled through the amplitude of the external pump field. It therefore provides an experimentally accessible coherent control parameter for tuning the phase structure while the cavity dissipation rate κ is kept fixed. The cavity and atomic detunings are defined as $\Delta_c = \omega_c - \omega_p/2$ and $\Delta_q = \omega_q - \omega_p/2$, respectively, where ω_c and ω_q denote the bare cavity-mode frequency and the atomic transition frequency, respectively.

For $G = 0$, the symmetry of the Hamiltonian is determined by the anisotropy of the light–matter coupling. Along the Tavis–Cummings line, $\lambda_x = \lambda_y$, the counterrotating terms vanish, and the total excitation number $\hat{\mathcal{N}} = a^\dagger a + S_z + N/2$ is conserved. The Hamiltonian is invariant under the continuous transformation $U(\theta) = e^{i\theta\hat{\mathcal{N}}}$, which gives rise to a $U(1)$ symmetry. Away from the Tavis–Cummings line, $\lambda_x \neq \lambda_y$, the counterrotating terms break excitation-number conservation, reducing the continuous $U(1)$ symmetry to the discrete Z_2 symmetry generated by $\Pi = e^{i\pi(a^\dagger a + S_z + N/2)}$. The parametric drive $G(a^2 + a^{\dagger 2})$ explicitly breaks the $U(1)$ symmetry even along the Tavis–Cummings line. Under the transformation $a \to e^{-i\theta}a$, the two-photon terms acquire phase factors $e^{\mp 2i\theta}$ and are therefore not invariant for a general θ. The discrete Z_2 symmetry, however, remains preserved because $a^2 + a^{\dagger 2}$ is invariant under $a \to -a$. Thus, the OPA reduces the continuous $U(1)$ symmetry to Z_2. Meanwhile, the parametric drive acts differently on the two cavity quadratures, which are governed by the effective coefficients $\Delta_c + 2G$ and $\Delta_c - 2G$, respectively. This quadrature-dependent renormalization provides the microscopic origin of the asymmetric deformation of the phase boundaries discussed below.

We now turn to the open-system dynamics by incorporating cavity photon loss. In contrast to the closed system, where the phase structure is determined solely by the effective Hamiltonian, the steady states of the driven–dissipative system arise from the competition between coherent light–matter interactions, parametric driving, and dissipation. Within the Markovian approximation, the system dynamics is governed by the Lindblad master equation

$$\dot{\rho} = -i[H_{\text{eff}}, \rho] + \kappa\Big(2a\rho a^\dagger - a^\dagger a\rho - \rho a^\dagger a\Big), \tag{2}$$

where κ denotes the cavity decay rate.

3. Steady-State Phase Diagram

To determine the steady-state phase structure, we first derive the semiclassical equations of motion. In the thermodynamic limit, we introduce the variables $\langle a\rangle = \sqrt{N}\alpha, \langle S_x\rangle = NX, \langle S_y\rangle = NY, \langle S_z\rangle = NZ$, where $\alpha = \alpha_{\text{Re}} + i\alpha_{\text{Im}}$. Factorizing mixed atom–field correlations as $\langle aS_\mu\rangle \simeq \langle a\rangle\langle S_\mu\rangle$, the equations of motion become

$$\dot{\alpha}_{\mathrm{Re}} = -\kappa\alpha_{\mathrm{Re}} + (\Delta_c - 2G)\alpha_{\mathrm{Im}} - 2\lambda_y Y, \tag{3a}$$
$$\dot{\alpha}_{\mathrm{Im}} = -(\Delta_c + 2G)\alpha_{\mathrm{Re}} - \kappa\alpha_{\mathrm{Im}} - 2\lambda_x X, \tag{3b}$$
$$\dot{X} = -\Delta_q Y - 4\lambda_y \alpha_{\mathrm{Im}} Z, \tag{3c}$$
$$\dot{Y} = \Delta_q X - 4\lambda_x \alpha_{\mathrm{Re}} Z, \tag{3d}$$
$$\dot{Z} = 4\lambda_x \alpha_{\mathrm{Re}} Y + 4\lambda_y \alpha_{\mathrm{Im}} X. \tag{3e}$$

The OPA introduces a quadrature-dependent modification of the semiclassical dynamics, with α_{Re} and α_{Im} governed by the effective coefficients $\Delta_c + 2G$ and $\Delta_c - 2G$, respectively.

The collective spin length is conserved within the mean-field approximation,

$$X^2 + Y^2 + Z^2 = \frac{1}{4}. \tag{4}$$

The steady states are obtained by setting the time derivatives in Equation (3) to zero together with the spin-length constraint. The normal-phase solution is

$$\alpha_{\mathrm{Re}} = \alpha_{\mathrm{Im}} = X = Y = 0, \qquad Z = -\frac{1}{2}. \tag{5}$$

For a superradiant steady state, eliminating the spin components from the stationary mean-field equations gives (see details in Appendix A.1)

$$\left(\Delta_c + 2G + \frac{8\lambda_x^2 Z}{\Delta_q}\right)\left(\Delta_c - 2G + \frac{8\lambda_y^2 Z}{\Delta_q}\right) + \kappa^2 = 0. \tag{6}$$

Solving for the spin polarization gives two formal branches,

$$Z_\pm = -\frac{\Delta_q}{16\lambda_x^2\lambda_y^2}\left[(\Delta_c + 2G)\lambda_y^2 + (\Delta_c - 2G)\lambda_x^2 \pm \sqrt{D}\right], \tag{7}$$

with

$$D = \left[(\Delta_c + 2G)\lambda_y^2 - (\Delta_c - 2G)\lambda_x^2\right]^2 - 4\kappa^2\lambda_x^2\lambda_y^2. \tag{8}$$

Mathematically, $D = 0$ determines the boundaries at which the two formal superradiant stationary branches coalesce. The physically relevant segments become discontinuous transition boundaries when the dynamically stable Z_- solution terminates with a finite order parameter, as confirmed by the linear-stability analysis in Appendix B and by the cuts shown below.

Real superradiant stationary solutions require $D \geq 0$. Introducing

$$\Xi = \sqrt{\kappa^2 + \Delta_c^2 - 4G^2}, \tag{9}$$

the condition $D = 0$ yields two branches,

$$\lambda_y = \frac{\Xi \pm \kappa}{\Delta_c + 2G}\lambda_x, \tag{10}$$

which together define the discontinuous (first-order) transition boundary. In addition to the phase boundaries, the analytic form of the superradiant solution changes across

$$\lambda_y = \lambda_x\sqrt{\frac{\Delta_c - 2G}{\Delta_c + 2G}}, \tag{11}$$

where the two analytic representations of the superradiant branch exchange their roles, as detailed in Appendix A.1. We refer to Equation (11) as the branch-exchange line; it does not by itself represent a phase-transition boundary.

Throughout this work, we restrict the parametric drive to the below-threshold regime $4G^2 < \Delta_c^2 + \kappa^2$, for which the uncoupled parametrically driven cavity possesses a stable stationary state. This condition also ensures that $\Xi = \sqrt{\kappa^2 + \Delta_c^2 - 4G^2}$ is real. All parameter sets considered below satisfy this condition. The continuous normal-to-superradiant transition is reached when the stable superradiant branch continuously merges with the normal state, i.e., when $Z_- \to -1/2$. Substituting $Z = -1/2$ into Equation (6) yields

$$\left(\Delta_c + 2G - \frac{4\lambda_x^2}{\Delta_q}\right)\left(\Delta_c - 2G - \frac{4\lambda_y^2}{\Delta_q}\right) + \kappa^2 = 0, \tag{12}$$

which determines the continuous (second-order) transition boundary. Solving Equation (12) for λ_y gives

$$\lambda_y = \frac{1}{2}\sqrt{\Delta_q\left[\Delta_c - 2G + \frac{\kappa^2\Delta_q}{(\Delta_c + 2G)\Delta_q - 4\lambda_x^2}\right]}. \tag{13}$$

Physical superradiant states are further constrained by dynamical stability. For the parameter regimes considered here, the Z_- branch is dynamically stable, whereas the Z_+ branch is unstable; see Appendix B. In the following, we retain only the stable Z_- branch.

To visualize the steady-state phase structure, we use the real and imaginary parts of the cavity field, α_{Re} and α_{Im}, as the superradiant order parameters. For a given stable polarization Z_-, these amplitudes are obtained from the stationary mean-field equations together with the spin-length constraint; their explicit expressions are given in Appendix A.1.

We now examine the mean-field phase structure in the (λ_x, λ_y) coupling plane. Figure 1a,b show the real and imaginary components of the cavity order parameter, α_{Re} and α_{Im}, respectively. The black dashed lines denote the first-order phase-transition boundaries, while the solid purple curves indicate the second-order transition boundaries. The two types of boundaries meet at the tricritical points, marked by red stars. For $G \neq 0$, the $\lambda_x \leftrightarrow \lambda_y$ exchange symmetry is explicitly broken, so that the diagonal $\lambda_x = \lambda_y$ no longer serves as a symmetry axis of the phase diagram. This asymmetry originates from the opposite OPA-induced shifts $\Delta_c + 2G$ and $\Delta_c - 2G$ of the two cavity quadratures. Consequently, the superradiant regions on the two sides of the diagonal become inequivalent.

The one-dimensional cuts in Figure 1c–f make the distinction between the continuous and discontinuous phase boundaries more explicit. For $\lambda_y/\Delta = 0.20$ [Figure 1c], both components of the cavity order parameter remain zero up to $\lambda_x/\Delta \simeq 0.596$ and then increase continuously from zero, indicating a continuous normal-to-superradiant transition. A similar behavior is observed for the complementary cut at $\lambda_x/\Delta = 0.30$ [Figure 1e], where the superradiant order parameter emerges continuously at $\lambda_y/\Delta \simeq 0.390$. In contrast, for $\lambda_y/\Delta = 0.50$ [Figure 1d], the initially superradiant state terminates abruptly at $\lambda_x/\Delta \simeq 0.685$, where both components of the order parameter drop discontinuously to zero. The system remains in the normal phase over a finite interval and reenters the superradiant phase through another discontinuous transition at $\lambda_x/\Delta \simeq 0.852$, yielding a characteristic SP–NP–SP sequence. Likewise, for $\lambda_x/\Delta = 0.59$ [Figure 1f], the order parameter exhibits a finite jump at $\lambda_y/\Delta \simeq 0.431$, providing direct signature of a discontinuous normal-to-superradiant transition.

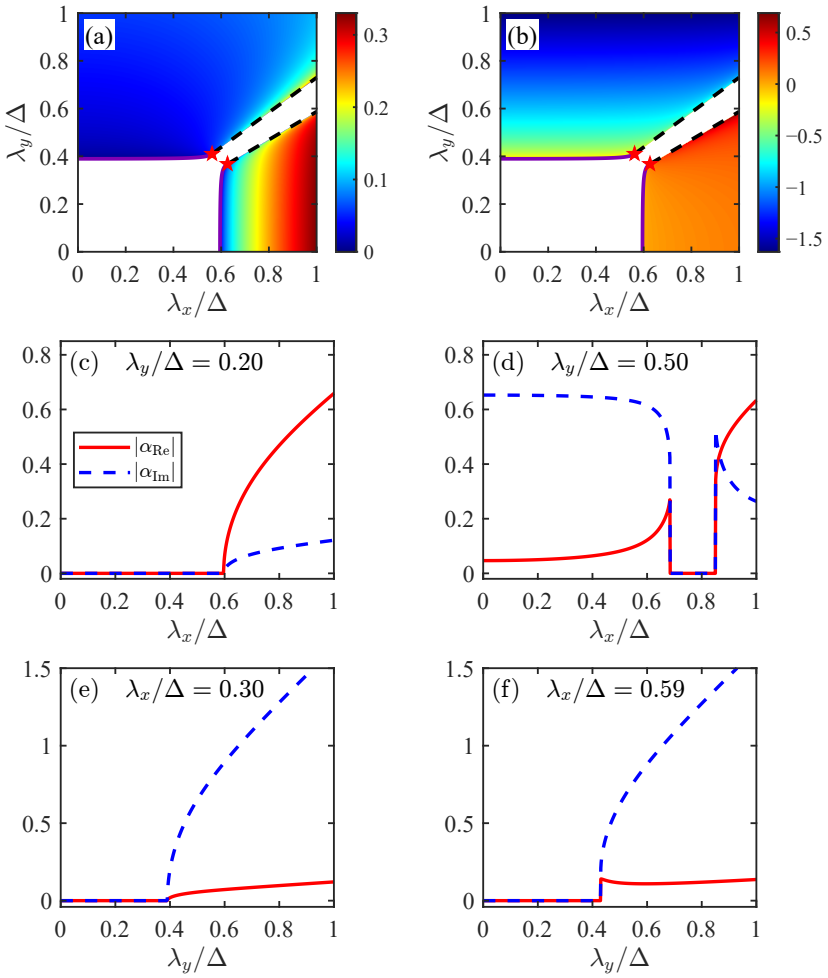


Figure 1. Mean-field phase diagram in the (λ_x, λ_y) plane. (**a**,**b**) Real and imaginary parts of the cavity order parameter, α_{Re} and α_{Im}, respectively. The black dashed lines indicate the first-order superradiant phase transition boundaries, and the solid purple curves denote the second-order phase transition boundary. The red stars indicate the tricritical points. The white region corresponds to the normal phase with $\alpha_{\mathrm{Re}} = \alpha_{\mathrm{Im}} = 0$. (**c**,**d**) Order parameters as functions of λ_x/Δ for fixed $\lambda_y/\Delta = 0.20$ and 0.50, respectively. (**e**,**f**) Corresponding cuts as functions of λ_y/Δ for fixed $\lambda_x/\Delta = 0.30$ and 0.59. Here $\Delta_c = \Delta_q = \Delta = 1$, $\kappa/\Delta = 0.1$, and $G/\Delta = 0.2$.

4. Tunable Tricritical Structure

The discontinuous boundaries in Equation (10) intersect the continuous boundary in Equation (13) at two tricritical points (TCPs). Using the definition of Ξ in Equation (9), their coordinates are

$$\begin{aligned} \lambda_x^{\mathrm{TCP1}} &= \frac{1}{2}\sqrt{\frac{(\Xi^2 + \kappa\Xi)\Delta_q}{\Delta_c - 2G}}, \\ \lambda_y^{\mathrm{TCP1}} &= \frac{\Xi - \kappa}{\Delta_c + 2G}\lambda_x^{\mathrm{TCP1}}, \end{aligned} \tag{14}$$

and

$$\begin{aligned} \lambda_x^{\mathrm{TCP2}} &= \frac{1}{2}\sqrt{\frac{(\Xi^2 - \kappa\Xi)\Delta_q}{\Delta_c - 2G}}, \\ \lambda_y^{\mathrm{TCP2}} &= \frac{\Xi + \kappa}{\Delta_c + 2G}\lambda_x^{\mathrm{TCP2}}. \end{aligned} \tag{15}$$

The detailed derivation of Equations (14) and (15) is given in Appendix A.2.

For $G = 0$ and finite cavity loss, the two tricritical points are related by the exchange $\lambda_x \leftrightarrow \lambda_y$, reflecting the symmetry of the dissipative IDTC model. A finite parametric drive removes this exchange symmetry and continuously deforms the tricritical pair in the (λ_x, λ_y) plane.

In the weak-loss limit $\kappa \to 0$, the two tricritical points coalesce at

$$\lambda_x^{(0)} = \frac{1}{2}\sqrt{(\Delta_c + 2G)\Delta_q}, \qquad \lambda_y^{(0)} = \frac{1}{2}\sqrt{(\Delta_c - 2G)\Delta_q}. \tag{16}$$

In the absence of parametric driving, $G = 0$, Equation (16) is reduced to $\lambda_x = \lambda_y = \lambda_c$, with $\lambda_c = \sqrt{\Delta_c \Delta_q}/2$.

Figure 2 illustrates the resulting evolution of the tricritical structure as the squeezing strength G is varied. At $G = 0$, the two tricritical points form a pair symmetric about the diagonal $\lambda_x = \lambda_y$. Increasing G breaks this symmetry: one tricritical point is displaced toward larger λ_x and smaller λ_y, whereas the other moves toward smaller λ_x and larger λ_y. Simultaneously, the branch-exchange line (denoted by the dashed line) in Equation (11) is shifted away from the diagonal. Therefore, the optical squeezing provides an independent control parameter for continuously reshaping the dissipation-induced multicritical structure.

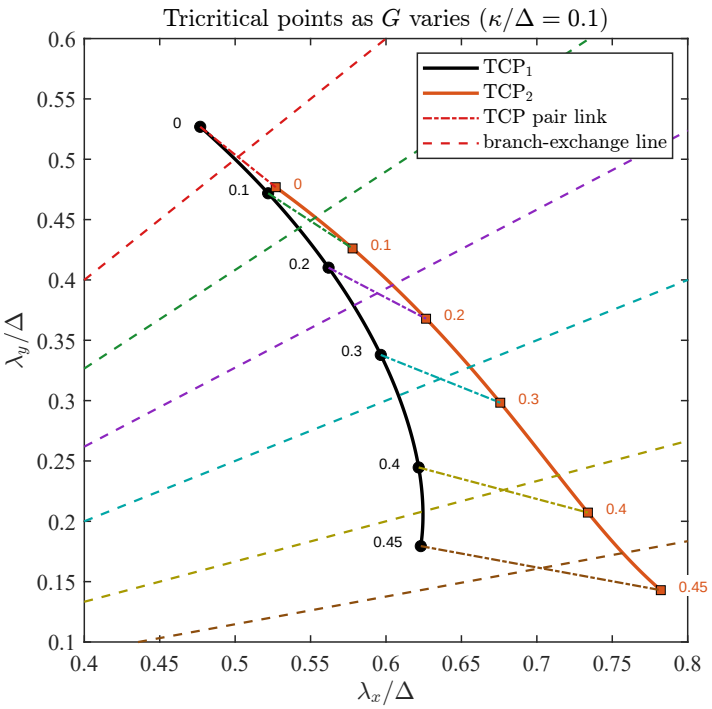


Figure 2. Evolution of the tricritical points in the (λ_x, λ_y) plane as the parametric-drive strength G is varied. The black circles and orange squares denote the trajectories of TCP$_1$ and TCP$_2$, respectively, with the adjacent numbers indicating G/Δ. For each value of G, the dot-dashed line connects the corresponding pair of tricritical points, while the dashed line indicates the branch-exchange line $\lambda_y/\lambda_x = \sqrt{(\Delta_c - 2G)/(\Delta_c + 2G)}$. The parameters are the same as in Figure 1.

The full control space is three dimensional, $(\lambda_x, \lambda_y, G)$. To visualize the pump-driven evolution while retaining both tricritical points in a single two-dimensional section, we introduce a fixed coupling-space trajectory:

$$\lambda_x \equiv \lambda, \qquad \lambda_y = k\lambda_x + c_0\Delta. \tag{17}$$

The line is chosen to pass through the two tricritical points at the reference parameters $G/\Delta = 0.20$, $\kappa/\Delta = 0.10$, and $\Delta_c = \Delta_q = \Delta$. This gives $k = -0.6547$, $c_0 = 0.7780$, as derived explicitly in Appendix A.2. Varying λ moves the system along this fixed trajectory in the

coupling plane, whereas varying G tracks the deformation of the phase structure induced by the parametric drive. Consequently, the original three-dimensional parameter space $(\lambda_x, \lambda_y, G)$ is represented by the reduced (λ, G) plane shown in Figure 3. Unless otherwise specified, $\Delta_c = \Delta_q = \Delta = 1$, $\kappa/\Delta = 0.1$, and $G/\Delta = 0.2$.

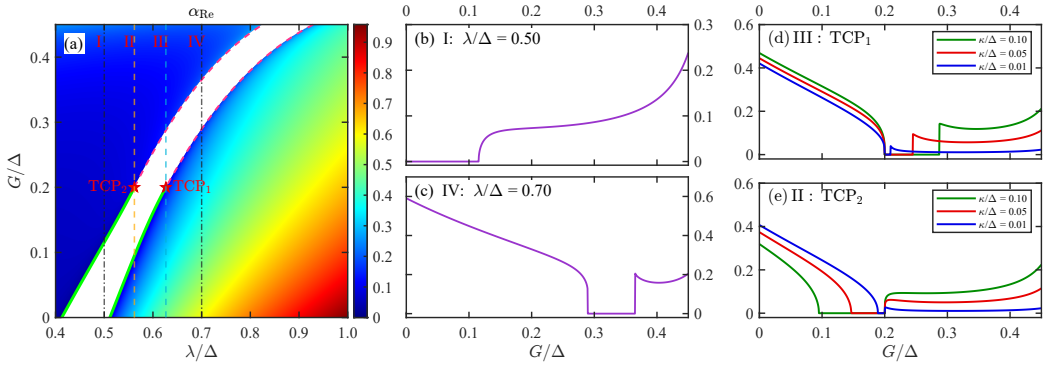


Figure 3. Mean-field order parameter in the (λ, G) plane along the linear cut defined in Equation (17). (**a**) Real part of the cavity order parameter, α_{Re}. The white region denotes the normal phase with $\alpha_{\mathrm{Re}} = 0$, while the colored regions correspond to superradiant solutions. The vertical dash-dotted lines labeled I–IV indicate representative values of λ/Δ, and the locations of TCP$_1$ and TCP$_2$ are marked by red stars. (**b**,**c**) Evolution of α_{Re} with the parametric-drive strength G at fixed $\lambda/\Delta = 0.50$ and 0.70, respectively. (**d**,**e**) Order-parameter profiles associated with TCP$_1$ and TCP$_2$ for different cavity decay rates $\kappa/\Delta = 0.10$, 0.05, and 0.01. Other parameters are the same as in Figure 1.

Figure 3a shows the real part of the cavity order parameter, α_{Re}, in the reduced (λ, G) plane along the linear trajectory defined in Equation (17). The white region corresponds to the normal phase, while a finite α_{Re} indicates the superradiant phase. The four vertical cuts I–IV are chosen according to their positions relative to the two tricritical points: cut I lies to the left of TCP$_2$, cuts II and III pass through the vicinity of TCP$_2$ and TCP$_1$, respectively, and cut IV lies to the right of TCP$_1$.

The corresponding one-dimensional cuts reveal qualitatively distinct behaviors. At $\lambda/\Delta = 0.50$ [Figure 3b], the cavity field remains zero at weak parametric driving and develops continuously beyond a critical value of G, indicating a transition from the normal to the superradiant phase. By contrast, for $\lambda/\Delta = 0.70$ [Figure 3c], the system is in superradiant phase at weak driving, enters a finite normal-phase window at intermediate G, and returns to a superradiant state upon further increasing the parametric strength. Thus, the OPA can either induce or suppress superradiance depending on the position along the coupling-space trajectory, leading to a characteristic reentrant SP–NP–SP structure.

The effect of cavity dissipation is further illustrated in Figure 3d,e, where λ is fixed at the values corresponding to TCP$_1$ and TCP$_2$, respectively, for the reference loss $\kappa/\Delta = 0.10$. For the TCP$_1$ cut [Figure 3d], a finite normal-phase window opens on the high-G side of the reference point $G/\Delta = 0.20$. As κ is reduced from 0.10 to 0.01, the upper boundary of this window moves toward $G/\Delta = 0.20$, so that the normal-phase interval progressively narrows. The complementary evolution is observed for the TCP$_2$ cut [Figure 3e]. Here the normal-phase window extends toward lower G, and decreasing κ shifts its lower boundary toward $G/\Delta = 0.20$. Thus, the normal-phase regions associated with the two tricritical points contract from opposite sides as the cavity loss is reduced. This behavior directly illustrates the dissipative origin of the splitting between the two tricritical points and their coalescence in the weak-loss limit.

5. Quantum Fluctuation Signatures

Having determined the stable mean-field steady states, we now investigate the quantum fluctuations around them. In the thermodynamic limit, the collective spin is represented by a Holstein–Primakoff boson b_s, $S_+ = b_s^\dagger\sqrt{N - b_s^\dagger b_s}, S_- = \sqrt{N - b_s^\dagger b_s}\, b_s$, $S_z = b_s^\dagger b_s - N/2$. We then expand the cavity and collective-spin fields around their mean-field values according to $a = \sqrt{N}\alpha + c, b_s = \sqrt{N}\beta + d$, where c and d describe the cavity and atomic quantum fluctuations, respectively. Because the mean-field amplitudes satisfy the steady-state equations, all linear terms in the fluctuation operators c and d vanish, leaving the terms of order N^0 to define the quadratic fluctuation Hamiltonian. Up to quadratic order, the fluctuation Hamiltonian can be written as

$$H_{\mathrm{fl}} = \Delta_c c^\dagger c + G\left(c^2 + c^{\dagger 2}\right) + \Omega_a d^\dagger d + \left(\Gamma_1 c^\dagger d + \Gamma_2 c d + \Gamma_3 d^{\dagger 2} + \mathrm{H.c.}\right), \tag{18}$$

where Ω_a and $\Gamma_{1,2,3}$ depend on the mean-field solution $(\alpha_{\mathrm{Re}}, \alpha_{\mathrm{Im}}, X, Y, Z)$. Their explicit expressions are given in Appendix C. The OPA contribution appears explicitly as the single-mode squeezing term $G(c^2 + c^{\dagger 2})$, and therefore modifies the cavity fluctuation spectrum.

To characterize the phase diagram in open-system dynamics, we use Heisenberg's equation of motion to obtain a closed set of ten linear equations for the second-order correlators: $\langle c^\dagger c\rangle$, $\langle c^2\rangle$, $\langle c^{\dagger 2}\rangle$, $\langle cd\rangle$, $\langle c^\dagger d^\dagger\rangle$, $\langle cd^\dagger\rangle$, $\langle c^\dagger d\rangle$, $\langle d^2\rangle$, $\langle d^{\dagger 2}\rangle$, and $\langle d^\dagger d\rangle$ (see Appendix D). Their stationary values are obtained by setting all ten time derivatives to zero. As a measure of the cavity fluctuations, we consider the photon number $\langle c^\dagger c\rangle$, where c denotes the fluctuation operator around the macroscopic cavity field. Figure 4a shows $\ln(\langle c^\dagger c\rangle + 1)$ in the reduced (λ, G) plane along the linear cut defined in Equation (17). The logarithmic scale is introduced to display the large variation of the fluctuation amplitude near the phase boundaries. Away from the critical regions, $\langle c^\dagger c\rangle$ remains small, while strong fluctuation enhancement occurs near the analytical phase boundaries.

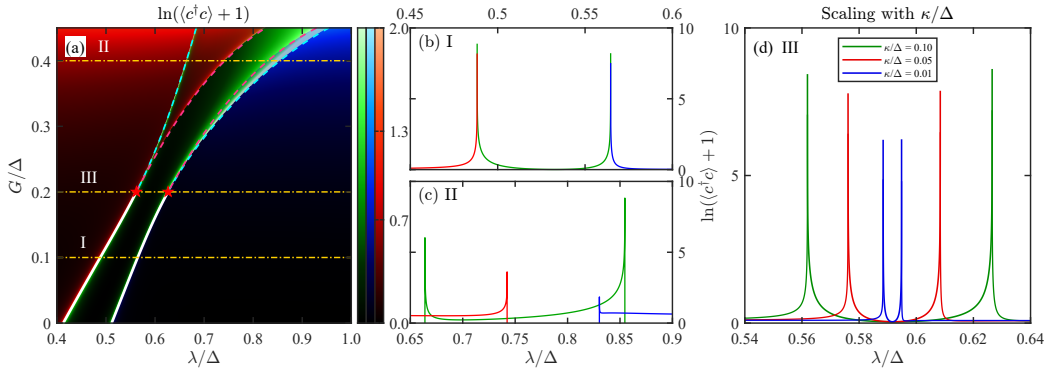


Figure 4. Photon-number fluctuations along the linear cut defined in Equation (17). (**a**) $\ln(\langle c^\dagger c\rangle + 1)$ in the (λ, G) plane. Separate color scales are used for the normal phase and the two superradiant branches. The dashed curves denote the first-order phase boundaries, while the solid white curves indicate the second-order phase boundaries. The horizontal lines mark cuts I–III at $G/\Delta = 0.10$, 0.40, and 0.20, respectively. (**b**,**c**) Photon-number fluctuations along cuts I and II, respectively. (**d**) Photon-number fluctuations along cut III for $\kappa/\Delta = 0.10$, 0.05, and 0.01. Other parameters are the same as in Figure 1.

Figure 4b,c further illustrate the fluctuation behavior across the two types of phase transitions. Along cut I [Figure 4b], the system crosses two second-order phase boundaries, at which the photon-number fluctuation is strongly enhanced and develops sharp peaks. These peak positions coincide with the continuous normal-to-superradiant transitions identified from the mean-field order parameter. In contrast, cut II [Figure 4c] crosses first-order phase boundaries. In this case, the fluctuation behavior changes abruptly across the transition points, consistent with the finite jumps of the mean-field order parameter.

The fluctuation profiles provide a clear distinction between the continuous and discontinuous transitions in the phase diagram.

The effect of cavity dissipation is illustrated in Figure 4d, where cut III is shown for several values of κ. For finite cavity loss, the two critical boundaries appear as two well-separated fluctuation peaks. As κ is reduced, the peaks move progressively toward one another and the interval between them becomes narrower. This evolution mirrors the shrinking normal-phase region found in the mean-field phase diagram and is consistent with the coalescence of the dissipation-induced tricritical structure in the weak-loss limit. Thus, the photon-number fluctuation provides a direct quantum signature of the dissipation-induced splitting and its coherent control by the parametric drive.

These signatures are directly relevant to experimental measurements. The cavity order parameter can be accessed through the coherent component of the output field. Through the standard input–output relation [43], the intracavity fluctuation quantity considered above is directly related to fluctuations of the cavity output field [8,44] and can be probed by photon counting or homodyne detection [45]. From an experimental perspective, the relevant signature is the displacement and enhancement of the fluctuation peaks as the parametric pump strength is varied. These output-field observables provide a possible route for identifying the squeezing-controlled evolution of the multicritical structure.

6. Conclusions

In summary, we have investigated the coherent control of dissipation-induced multicriticality in the interpolating Dicke–Tavis–Cummings model by intracavity optical squeezing. The parametric interaction acts differently on the two cavity quadratures and thereby provides a coherent method for continuously reshaping this loss-generated tricritical structure. Within the mean-field approximation, we obtained the steady-state solutions and the corresponding phase boundaries analytically. We showed that the parametric drive continuously displaces the dissipation-induced pair of tricritical points whose positions can be controlled by the pump strength. We further studied quantum fluctuations around the stable mean-field steady states using a Holstein–Primakoff expansion and the corresponding quadratic fluctuation dynamics. The intracavity parametric interaction enters directly as a single-mode squeezing term in the fluctuation Hamiltonian and strongly modifies the cavity fluctuation spectrum.

Author Contributions: Conceptualization, Y.H. and G.-L.Z.; methodology, Y.H. and G.-L.Z.; software, Y.H.; writing—original draft preparation, Y.H. and G.-L.Z.; writing—review and editing, L.C., G.-L.Z. and X.W.; supervision, G.-L.Z. and L.C.; funding acquisition, project administration, G.-L.Z. and X.W. All authors have read and agreed to the published version of the manuscript.

Funding: This work is supported by the National Natural Science Foundation of China (Grant No. 12405027), the Zhejiang Provincial Natural Science Foundation of China (Grant No. LQN25A050001), the Quantum Science and Technology–National Science and Technology Major Project (Grant No. 2024ZD0301000), and the Science Foundation of Zhejiang Sci-Tech University (Grant Nos. 24062156-Y and 23062088-Y).

Data Availability Statement: The data supporting the findings of this study are available from the corresponding authors upon reasonable request.

Conflicts of Interest: The authors declare no conflicts of interest.

Abbreviations

The following abbreviations are used in this manuscript:

IDTC	Interpolating Dicke–Tavis–Cummings
OPA	Optical parametric amplification
NP	Normal phase
SP	Superradiant phase
TCP	Tricritical point

Appendix A. Mean-Field Steady States and Tricritical Structure

This Appendix presents the derivation of the explicit superradiant steady-state amplitudes and the associated branch-exchange condition. We then derive the coordinates of the two tricritical points and construct the linear trajectory used in the reduced (λ, G) phase diagrams.

Appendix A.1. Explicit Superradiant Amplitudes and Branch Exchange

For a chosen polarization Z satisfying Equation (7), the stationary spin equations give

$$X = \frac{4\lambda_x Z}{\Delta_q}\alpha_{\mathrm{Re}}, \qquad Y = -\frac{4\lambda_y Z}{\Delta_q}\alpha_{\mathrm{Im}}. \tag{A1}$$

The stationary cavity equations provide an equivalent expression,

$$X = -\frac{(\Delta_c + 2G)\alpha_{\mathrm{Re}} + \kappa\alpha_{\mathrm{Im}}}{2\lambda_x}, \tag{A2}$$

$$Y = \frac{(\Delta_c - 2G)\alpha_{\mathrm{Im}} - \kappa\alpha_{\mathrm{Re}}}{2\lambda_y}. \tag{A3}$$

It is useful to define

$$Q \equiv \frac{1}{4} - Z^2. \tag{A4}$$

Using the spin-length constraint Equation (4) gives

$$Q = a_1\alpha_{\mathrm{Re}}^2 + a_2\alpha_{\mathrm{Im}}^2, \tag{A5}$$

where

$$a_1 = \frac{16Z^2\lambda_x^2}{\Delta_q^2}, \qquad a_2 = \frac{16Z^2\lambda_y^2}{\Delta_q^2}. \tag{A6}$$

Alternatively, using Equation (A3), one obtains

$$Q = b_1\alpha_{\mathrm{Re}}^2 + b_2\alpha_{\mathrm{Re}}\alpha_{\mathrm{Im}} + b_3\alpha_{\mathrm{Im}}^2, \tag{A7}$$

with

$$b_1 = \frac{1}{4}\left[\frac{(\Delta_c + 2G)^2}{\lambda_x^2} + \frac{\kappa^2}{\lambda_y^2}\right], \tag{A8a}$$

$$b_2 = \frac{\kappa}{2}\left[\frac{\Delta_c + 2G}{\lambda_x^2} - \frac{\Delta_c - 2G}{\lambda_y^2}\right], \tag{A8b}$$

$$b_3 = \frac{1}{4}\left[\frac{\kappa^2}{\lambda_x^2} + \frac{(\Delta_c - 2G)^2}{\lambda_y^2}\right]. \tag{A8c}$$

Subtracting Equations (A5) and (A7), and defining

$$r \equiv \frac{\alpha_{\mathrm{Im}}}{\alpha_{\mathrm{Re}}}, \tag{A9}$$

gives

$$(a_2 - b_3)r^2 - b_2 r + (a_1 - b_1) = 0. \tag{A10}$$

The two analytic ratios are therefore

$$r_\pm = \frac{b_2 \pm \sqrt{b_2^2 - 4(a_2 - b_3)(a_1 - b_1)}}{2(a_2 - b_3)}. \tag{A11}$$

For either analytic branch, the cavity amplitudes can then be written compactly as

$$\alpha_{\mathrm{Re}} = \sigma\sqrt{\frac{Q}{a_1 + a_2 r_\pm^2}}, \qquad \alpha_{\mathrm{Im}} = r_\pm \alpha_{\mathrm{Re}}, \qquad \sigma = \pm 1. \tag{A12}$$

The two values of σ are related by the $\mathbb{Z}_2$ parity symmetry and therefore describe the degenerate pair of symmetry-broken steady states. The associated spin components follow directly from Equation (A1). In the parameter regimes used in the main text, dynamical stability selects the Z_- polarization branch together with the appropriate analytic continuation of Equation (A11); see Appendix B.

The mixed coefficient b_2 controls the coupling between the two cavity quadratures in Equation (A7). For finite cavity loss, the two analytic superradiant continuations exchange their labeling when this mixed term vanishes,

$$b_2 = 0. \tag{A13}$$

Using Equation (A8b), this condition becomes

$$\frac{\Delta_c + 2G}{\lambda_x^2} = \frac{\Delta_c - 2G}{\lambda_y^2}, \tag{A14}$$

or

$$\lambda_y = \lambda_x\sqrt{\frac{\Delta_c - 2G}{\Delta_c + 2G}}, \tag{A15}$$

which reproduces the branch-exchange line Equation (11) in the main text.

Appendix A.2. Tricritical Points and Construction of the Linear Cut

The tricritical points are obtained by intersecting the two superradiant-existence boundaries with the continuous normal-to-superradiant boundary. For compactness, define

$$A \equiv \Delta_c + 2G, \qquad B \equiv \Delta_c - 2G, \qquad \Xi = \sqrt{\kappa^2 + AB}. \tag{A16}$$

The two branches of the existence boundary, Equation (10), can then be parameterized as

$$\lambda_y = m_s \lambda_x, \qquad m_s = \frac{\Xi + s\kappa}{A}, \qquad s = \pm 1. \tag{A17}$$

Substituting Equation (A17) into the continuous-boundary condition, Equation (12), gives

$$\left(\lambda_x^{(s)}\right)^2 = \frac{\Xi(\Xi - s\kappa)\Delta_q}{4B}, \qquad \lambda_y^{(s)} = \frac{\Xi + s\kappa}{A}\lambda_x^{(s)}. \tag{A18}$$

The choice $s = -1$ gives TCP1, whereas $s = +1$ gives TCP2. Equation (A18) therefore reproduces Equations (14) and (15) of the main text.

Several limiting cases follow immediately. For $G = 0$, $A = B = \Delta_c$, and the two points satisfy

$$\lambda_x^{\mathrm{TCP1}} = \lambda_y^{\mathrm{TCP2}}, \qquad \lambda_y^{\mathrm{TCP1}} = \lambda_x^{\mathrm{TCP2}}, \tag{A19}$$

so that the tricritical pair is symmetric about $\lambda_x = \lambda_y$ for finite κ.

In the weak-loss limit,

$$\kappa \to 0, \qquad \Xi \to \sqrt{AB}, \tag{A20}$$

the two solutions of Equation (A18) coalesce at

$$\lambda_x = \frac{1}{2}\sqrt{A\Delta_q}, \qquad \lambda_y = \frac{1}{2}\sqrt{B\Delta_q}, \tag{A21}$$

which is Equation (16). For $G = 0$ this further reduces to $\lambda_x = \lambda_y = \sqrt{\Delta_c\Delta_q}/2$.

We finally construct the linear trajectory used in Figures 3 and 4. For the reference parameters $G/\Delta = 0.20$, $\kappa/\Delta = 0.10$, and $\Delta_c = \Delta_q = \Delta$, Equations (14) and (15) give

$$\frac{(\lambda_x^{\mathrm{TCP1}}, \lambda_y^{\mathrm{TCP1}})}{\Delta} \simeq (0.6266, 0.3679), \tag{A22}$$

and

$$\frac{(\lambda_x^{\mathrm{TCP2}}, \lambda_y^{\mathrm{TCP2}})}{\Delta} \simeq (0.5619, 0.4102). \tag{A23}$$

The slope of the straight line passing through these two points is therefore

$$k = \frac{\lambda_y^{\mathrm{TCP2}} - \lambda_y^{\mathrm{TCP1}}}{\lambda_x^{\mathrm{TCP2}} - \lambda_x^{\mathrm{TCP1}}} \simeq -0.6547, \tag{A24}$$

and its dimensionless intercept is

$$c_0 = \frac{\lambda_y^{\mathrm{TCP1}}}{\Delta} - k\frac{\lambda_x^{\mathrm{TCP1}}}{\Delta} \simeq 0.7780. \tag{A25}$$

Hence the fixed trajectory is

$$\lambda_x \equiv \lambda, \qquad \lambda_y = k\lambda_x + c_0\Delta, \tag{A26}$$

which is Equation (17) in the main text.

Appendix B. Linear Stability Analysis

Let each mean-field variable be written as its stationary value plus a small fluctuation. The spin constraint eliminates the longitudinal component:

$$\delta Z = -\frac{X\delta X + Y\delta Y}{Z}. \tag{A27}$$

For $\boldsymbol{f} = (\delta\alpha_{\mathrm{Re}}, \delta\alpha_{\mathrm{Im}}, \delta X, \delta Y)^T$, the linearized dynamics is $\dot{\boldsymbol{f}} = M_{\mathrm{st}}\boldsymbol{f}$, where

$$M_{\mathrm{st}} = \begin{pmatrix} -\kappa & \Delta_c - 2G & 0 & -2\lambda_y \\ -(\Delta_c + 2G) & -\kappa & -2\lambda_x & 0 \\ 0 & -4\lambda_y Z & 4\lambda_y\alpha_{\mathrm{Im}}X/Z & -\Delta_q + 4\lambda_y\alpha_{\mathrm{Im}}Y/Z \\ -4\lambda_x Z & 0 & \Delta_q + 4\lambda_x\alpha_{\mathrm{Re}}X/Z & 4\lambda_x\alpha_{\mathrm{Re}}Y/Z \end{pmatrix}. \tag{A28}$$

A fixed point is linearly stable when every eigenvalue μ_j of $M_{\rm st}$ satisfies $\mathrm{Re}\,\mu_j < 0$; a phase boundary is reached when the largest real part becomes zero.

For the normal fixed point $(\alpha_{\rm Re}, \alpha_{\rm Im}, X, Y, Z) = (0, 0, 0, 0, -1/2)$, Equation (A28) reduces to

$$M_{\rm NP} = \begin{pmatrix} -\kappa & \Delta_c - 2G & 0 & -2\lambda_y \\ -(\Delta_c + 2G) & -\kappa & -2\lambda_x & 0 \\ 0 & 2\lambda_y & 0 & -\Delta_q \\ 2\lambda_x & 0 & \Delta_q & 0 \end{pmatrix}. \tag{A29}$$

For a superradiant phase, the solutions in Equation (A12) are substituted into Equation (A28) before diagonalization. Figure A1 shows the linear stability in (λ, G) plane. The normal-phase solution is stable only in the finite region shown in Figure A1a, and the stability of the superradiant phase is shown in Figure A1b. The boundaries of these regions are determined by the condition $\max \mathrm{Re}(\mu_j) = 0$, where μ_j are the eigenvalues of the linearized stability matrix. In particular, the loss-induced normal-phase strip identified from the stability analysis agrees closely with that obtained from the mean-field order parameter.

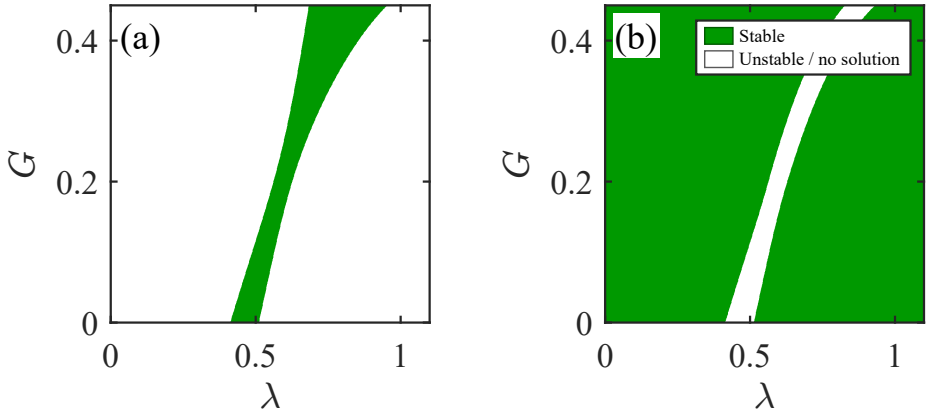


Figure A1. Linear-stability diagrams in the (λ, G) plane for (**a**) the normal phase and (**b**) the superradiant Z_- branch. Green regions indicate dynamically stable steady states, for which all eigenvalues of the corresponding stability matrix have negative real parts. White regions denote parameter regimes where the considered steady state is unstable. Only the Z_- superradiant branch is shown in panel (**b**), since the Z_+ branch is unstable in the parameter regime considered.

Throughout this work, we use the Z_- branch to construct the mean-field phase diagrams and the corresponding fluctuation spectra. As confirmed by the linear-stability analysis, the Z_- solutions are dynamically stable in the parameter regimes considered in Figures 3 and 4. By contrast, whenever the Z_+ branch satisfies the spin constraint, it possesses at least one eigenvalue with a positive real part and is therefore dynamically unstable. The Z_+ branch is thus excluded from the physical phase diagrams and is not shown.

Appendix C. Holstein–Primakoff Expansion and Fluctuation Coefficients

For a collective spin of length $S = N/2$, we introduce a Holstein–Primakoff boson b_s through

$$\begin{aligned} S_+ &= b_s^\dagger \sqrt{N - b_s^\dagger b_s}, \qquad S_- = \sqrt{N - b_s^\dagger b_s}\, b_s, \\ S_z &= -\frac{N}{2} + b_s^\dagger b_s. \end{aligned} \tag{A30}$$

We displace the cavity and atomic bosons according to

$$a = \sqrt{N}\alpha + c, \qquad b_s = \sqrt{N}\beta + d. \tag{A31}$$

Expanding the square root in Equation (A30) in powers of $N^{-1/2}$, the terms of order $N^{1/2}$ vanish when the mean-field equations are satisfied. The terms of order N^0 give Equation (18). For the convention in Equation (A31), its coefficients are

$$\Omega_a = \frac{(1-2Z)^2\Delta_q - 2\lambda_y Y(-5+6Z)\alpha_{\mathrm{Im}} + 2\lambda_x X(-5+6Z)\alpha_{\mathrm{Re}}}{(1-2Z)^2}, \tag{A32a}$$

$$\Gamma_1 = \frac{\lambda_x[4X(X+iY) - (1-2Z)^2] + \lambda_y[-4Y(iX-Y) - (1-2Z)^2]}{\sqrt{2-4Z}(-1+2Z)}, \tag{A32b}$$

$$\Gamma_2 = \frac{\lambda_x[4X(X+iY) - (1-2Z)^2] + \lambda_y[4iXY - 4Y^2 + (1-2Z)^2]}{\sqrt{2-4Z}(-1+2Z)}, \tag{A32c}$$

$$\Gamma_3 = \frac{2(X-iY)}{(-1+2Z)^3}\Big\{[-2XY + i(2Y^2 + (1-2Z)^2)]\lambda_y\alpha_{\mathrm{Im}} + [2X(X-iY) + (1-2Z)^2]\lambda_x\alpha_{\mathrm{Re}}\Big\}. \tag{A32d}$$

At the normal fixed point $(X, Y, Z, \alpha) = (0, 0, -1/2, 0)$, these expressions reduce to

$$\begin{aligned} \Omega_a &= \Delta_q, & \Gamma_1 &= \lambda_x + \lambda_y, \\ \Gamma_2 &= \lambda_x - \lambda_y, & \Gamma_3 &= 0. \end{aligned} \tag{A33}$$

The OPA term contributes directly to the quadratic fluctuation Hamiltonian through $G(c^2 + c^{\dagger 2})$. The remaining coefficients retain the same functional structure as in the IDTC model, but depend implicitly on G through the G-dependent mean-field steady state.

Appendix D. Equations of Motion for Second-Order Correlations

The equal-time two-operator correlators are obtained directly from Heisenberg's equation of motion. For example, the cavity photon-number operator obeys

$$\frac{d}{dt}\Big[c^\dagger(t)c(t)\Big] = -i\Big[H_{\mathrm{fl}}, c^\dagger(t)c(t)\Big] - 2\kappa c^\dagger(t)c(t), \tag{A34}$$

where $\hbar = 1$, and the last term accounts for cavity loss. Evaluating the corresponding commutator for each two-operator product gives the following closed equations of motion:

$$\frac{d}{dt}\langle c^\dagger c\rangle = -2\kappa\langle c^\dagger c\rangle - i\Gamma_1\langle c^\dagger d\rangle + i\Gamma_1^*\langle cd^\dagger\rangle + i\Gamma_2\langle cd\rangle - i\Gamma_2^*\langle c^\dagger d^\dagger\rangle + 2iG\Big(\langle c^2\rangle - \langle c^{\dagger 2}\rangle\Big), \tag{A35a}$$

$$\frac{d}{dt}\langle c^2\rangle = -2(i\Delta_c + \kappa)\langle c^2\rangle - 2i\Gamma_1\langle cd\rangle - 2i\Gamma_2^*\langle cd^\dagger\rangle - 2iG\Big(2\langle c^\dagger c\rangle + 1\Big), \tag{A35b}$$

$$\frac{d}{dt}\langle c^{\dagger 2}\rangle = 2(i\Delta_c - \kappa)\langle c^{\dagger 2}\rangle + 2i\Gamma_1^*\langle c^\dagger d^\dagger\rangle + 2i\Gamma_2\langle c^\dagger d\rangle + 2iG\Big(2\langle c^\dagger c\rangle + 1\Big), \tag{A35c}$$

$$\frac{d}{dt}\langle cd\rangle = -(i\Delta_c + \kappa + i\Omega_a)\langle cd\rangle - i\Gamma_1^*\langle c^2\rangle - i\Gamma_1\langle d^2\rangle - i\Gamma_2^*\Big(\langle c^\dagger c\rangle + \langle d^\dagger d\rangle + 1\Big) - 2i\Gamma_3\langle cd^\dagger\rangle - 2iG\langle c^\dagger d\rangle, \tag{A35d}$$

$$\frac{d}{dt}\langle c^\dagger d^\dagger\rangle = (i\Delta_c - \kappa + i\Omega_a)\langle c^\dagger d^\dagger\rangle + i\Gamma_1\langle c^{\dagger 2}\rangle + i\Gamma_1^*\langle d^{\dagger 2}\rangle + i\Gamma_2\Big(\langle c^\dagger c\rangle + \langle d^\dagger d\rangle + 1\Big) + 2i\Gamma_3^*\langle c^\dagger d\rangle + 2iG\langle cd^\dagger\rangle, \tag{A35e}$$

$$\frac{d}{dt}\langle cd^\dagger\rangle = i(\Omega_a - \Delta_c + i\kappa)\langle cd^\dagger\rangle + i\Gamma_1\Big(\langle c^\dagger c\rangle - \langle d^\dagger d\rangle\Big) + i\Gamma_2\langle c^2\rangle - i\Gamma_2^*\langle d^{\dagger 2}\rangle + 2i\Gamma_3^*\langle cd\rangle - 2iG\langle c^\dagger d^\dagger\rangle, \tag{A35f}$$

$$\frac{d}{dt}\langle c^\dagger d\rangle = i(\Delta_c - \Omega_a + i\kappa)\langle c^\dagger d\rangle - i\Gamma_1^*\Big(\langle c^\dagger c\rangle - \langle d^\dagger d\rangle\Big) - i\Gamma_2^*\langle c^{\dagger 2}\rangle + i\Gamma_2\langle d^2\rangle - 2i\Gamma_3\langle c^\dagger d^\dagger\rangle + 2iG\langle cd\rangle, \tag{A35g}$$

$$\frac{d}{dt}\langle d^2\rangle = -2i\Omega_a\langle d^2\rangle - 2i\Gamma_1^*\langle cd\rangle - 2i\Gamma_2^*\langle c^\dagger d\rangle - 2i\Gamma_3\Big(2\langle d^\dagger d\rangle + 1\Big), \tag{A35h}$$

$$\frac{d}{dt}\langle d^{\dagger 2}\rangle = 2i\Omega_a\langle d^{\dagger 2}\rangle + 2i\Gamma_1\langle c^\dagger d^\dagger\rangle + 2i\Gamma_2\langle cd^\dagger\rangle + 2i\Gamma_3^*\Big(2\langle d^\dagger d\rangle + 1\Big), \tag{A35i}$$

$$\frac{d}{dt}\langle d^\dagger d\rangle = i\Gamma_1\langle c^\dagger d\rangle - i\Gamma_1^*\langle cd^\dagger\rangle + i\Gamma_2\langle cd\rangle - i\Gamma_2^*\langle c^\dagger d^\dagger\rangle - 2i\Gamma_3\langle d^{\dagger 2}\rangle + 2i\Gamma_3^*\langle d^2\rangle. \tag{A35j}$$

https://doi.org/10.3390/photonics13090885

The constant terms appearing in Equations (A35a)–(A35j) originate from the bosonic commutation relations, such as $cc^\dagger = c^\dagger c + 1$. For each stable mean-field steady state, we first evaluate the corresponding coefficients Ω_a and $\Gamma_{1,2,3}$ and collect the ten second-order correlators into the vector

$$\mathbf{v} = \left(\langle c^\dagger c\rangle, \langle c^2\rangle, \langle c^{\dagger 2}\rangle, \langle cd\rangle, \langle c^\dagger d^\dagger\rangle, \langle cd^\dagger\rangle, \langle c^\dagger d\rangle, \langle d^2\rangle, \langle d^{\dagger 2}\rangle, \langle d^\dagger d\rangle\right)^T. \tag{A36}$$

The coupled Equations (A35a)–(A35j) can be written in the compact linear form

$$\dot{\mathbf{v}} = \mathbf{M}_{\mathrm{fl}}\mathbf{v} + \mathbf{s}, \tag{A37}$$

where $\mathbf{M}_{\mathrm{fl}}$ is determined by the fluctuation coefficients and $\mathbf{s}$ contains the constant terms generated by the bosonic commutators. In the stationary state, $\dot{\mathbf{v}} = 0$, and the correlation functions are obtained by solving

$$\mathbf{M}_{\mathrm{fl}}\mathbf{v}_{\mathrm{ss}} = -\mathbf{s}. \tag{A38}$$

The cavity photon-number fluctuation $\langle c^\dagger c\rangle$ is then extracted from the first component of $\mathbf{v}_{\mathrm{ss}}$.

References

1. Sachdev, S. *Quantum Phase Transitions*; Cambridge University Press: Cambridge, UK, 2011.
2. Domb, C. *Phase Transitions and Critical Phenomena*; Elsevier: Amsterdam, The Netherlands, 2000.
3. Dicke, R.H. Coherence in Spontaneous Radiation Processes. *Phys. Rev.* **1954**, *93*, 99–110. [CrossRef]
4. Tavis, M.; Cummings, F.W. Exact Solution for an *N*-Molecule—Radiation-Field Hamiltonian. *Phys. Rev.* **1968**, *170*, 379–384. [CrossRef]
5. Wang, Y.K.; Hioe, F.T. Phase Transition in the Dicke Model of Superradiance. *Phys. Rev. A* **1973**, *7*, 831–836. [CrossRef]
6. Hioe, F.T. Phase Transitions in Some Generalized Dicke Models of Superradiance. *Phys. Rev. A* **1973**, *8*, 1440–1445. [CrossRef]
7. Emary, C.; Brandes, T. Chaos and the quantum phase transition in the Dicke model. *Phys. Rev. E* **2003**, *67*, 066203. [CrossRef]
8. Dimer, F.; Estienne, B.; Parkins, A.S.; Carmichael, H.J. Proposed realization of the Dicke-model quantum phase transition in an optical cavity QED system. *Phys. Rev. A* **2007**, *75*, 013804. [CrossRef]
9. Nagy, D.; Kónya, G.; Szirmai, G.; Domokos, P. Dicke-Model Phase Transition in the Quantum Motion of a Bose-Einstein Condensate in an Optical Cavity. *Phys. Rev. Lett.* **2010**, *104*, 130401. [CrossRef]
10. Baden, M.P.; Arnold, K.J.; Grimsmo, A.L.; Parkins, S.; Barrett, M.D. Realization of the Dicke Model Using Cavity-Assisted Raman Transitions. *Phys. Rev. Lett.* **2014**, *113*, 020408. [CrossRef]
11. Zhang, G.Q.; Chen, Z.; You, J.Q. Experimentally accessible quantum phase transition in a non-Hermitian Tavis-Cummings model engineered with two drive fields. *Phys. Rev. A* **2020**, *102*, 032202. [CrossRef]
12. Chen, X.Y.; Zhang, Y.Y.; Chen, Q.H.; Lin, H.Q. Phase transitions in the anisotropic Dicke-Stark model with A^2 terms. *Phys. Rev. A* **2024**, *110*, 063722. [CrossRef]
13. Zhang, Y.Y.; Hu, Z.X.; Fu, L.; Luo, H.G.; Pu, H.; Zhang, X.F. Quantum Phases in a Quantum Rabi Triangle. *Phys. Rev. Lett.* **2021**, *127*, 063602. [CrossRef]
14. Zheng, R.H.; Ning, W.; Chen, Y.H.; Lü, J.H.; Shen, L.T.; Xu, K.; Zhang, Y.-R.; Xu, D.; Li, H.; Xia, Y.; et al. Observation of a Superradiant Phase Transition with Emergent Cat States. *Phys. Rev. Lett.* **2023**, *131*, 113601. [CrossRef]
15. Xu, Y.; Pu, H. Emergent Universality in a Quantum Tricritical Dicke Model. *Phys. Rev. Lett.* **2019**, *122*, 193201. [CrossRef]
16. Zhu, H.J.; Xu, K.; Zhang, G.F.; Liu, W.M. Finite-Component Multicriticality at the Superradiant Quantum Phase Transition. *Phys. Rev. Lett.* **2020**, *125*, 050402. [CrossRef]
17. Xu, Y.; Fallas Padilla, D.; Pu, H. Multicriticality and quantum fluctuation in a generalized Dicke model. *Phys. Rev. A* **2021**, *104*, 043708. [CrossRef]
18. Ying, Z.J. Symmetry-breaking patterns, tricriticalities, and quadruple points in the quantum Rabi model with bias and nonlinear interaction. *Phys. Rev. A* **2021**, *103*, 063701. [CrossRef]
19. Cheng, J.M.; Zhang, Y.C.; Zhou, X.F.; Zhou, Z.W. Super-Heisenberg Scaling in a Triple-Point Criticality. *Phys. Rev. Lett.* **2025**, *134*, 190802. [CrossRef]

20. Wang, T.L.; Wu, L.N.; Yang, W.; Jin, G.R.; Lambert, N.; Nori, F. Quantum Fisher information as a signature of the superradiant quantum phase transition. *New J. Phys.* **2014**, *16*, 063039. [CrossRef]
21. Frérot, I.; Roscilde, T. Quantum Critical Metrology. *Phys. Rev. Lett.* **2018**, *121*, 020402. [CrossRef]
22. Friedemann, S.; Duncan, W.J.; Hirschberger, M.; Bauer, T.W.; Küchler, R.; Neubauer, A.; Brando, M.; Pfleiderer, C.; Grosche, F.M. Quantum tricritical points in NbFe. *Nat. Phys.* **2018**, *14*, 62–67. [CrossRef]
23. Ying, Z.J.; Felicetti, S.; Liu, G.; Braak, D. Critical Quantum Metrology in the Non-Linear Quantum Rabi Model. *Entropy* **2022**, *24*, 1015. [CrossRef]
24. He, W.T.; Lu, C.W.; Yao, Y.X.; Zhu, H.Y.; Ai, Q. Criticality-based quantum metrology in the presence of decoherence. *Front. Phys.* **2023**, *18*, 31304. [CrossRef]
25. Hotter, C.; Ritsch, H.; Gietka, K. Combining Critical and Quantum Metrology. *Phys. Rev. Lett.* **2024**, *132*, 060801. [CrossRef]
26. Zhu, X.; Lü, J.H.; Ning, W.; Shen, L.T.; Wu, F.; Yang, Z.B. Quantum geometric tensor and critical metrology in the anisotropic Dicke model. *Phys. Rev. A* **2024**, *109*, 052621. [CrossRef]
27. Baksic, A.; Ciuti, C. Controlling Discrete and Continuous Symmetries in "Superradiant" Phase Transitions with Circuit QED Systems. *Phys. Rev. Lett.* **2014**, *112*, 173601. [CrossRef]
28. Kirton, P.; Keeling, J. Suppressing and Restoring the Dicke Superradiance Transition by Dephasing and Decay. *Phys. Rev. Lett.* **2017**, *118*, 123602. [CrossRef]
29. Soriente, M.; Donner, T.; Chitra, R.; Zilberberg, O. Dissipation-Induced Anomalous Multicritical Phenomena. *Phys. Rev. Lett.* **2018**, *120*, 183603. [CrossRef]
30. Lin, R.; Rosa-Medina, R.; Ferri, F.; Finger, F.; Kroeger, K.; Donner, T.; Esslinger, T.; Chitra, R. Dissipation-Engineered Family of Nearly Dark States in Many-Body Cavity-Atom Systems. *Phys. Rev. Lett.* **2022**, *128*, 153601. [CrossRef]
31. Wu, Z.; Hu, C.; Wang, T.; Chen, Y.; Li, Y.; Zhao, L.; Lü, X.Y.; Peng, X. Experimental Quantum Simulation of Multicriticality in Closed and Open Rabi Model. *Phys. Rev. Lett.* **2024**, *133*, 173602. [CrossRef]
32. Xu, Y.J.; Zhai, L.H.; Fu, P.; Cheng, S.J.; Zhang, G.Q. Nonreciprocal quantum phase transition in cavity magnonics. *Phys. Rev. A* **2024**, *110*, 043704. [CrossRef]
33. Kirton, P.; Roses, M.M.; Keeling, J.; Dalla Torre, E.G. Introduction to the Dicke Model: From Equilibrium to Nonequilibrium, and Vice Versa. *Adv. Quantum Technol.* **2019**, *2*, 1800043. [CrossRef]
34. Zhu, C.J.; Ping, L.L.; Yang, Y.P.; Agarwal, G.S. Squeezed Light Induced Symmetry Breaking Superradiant Phase Transition. *Phys. Rev. Lett.* **2020**, *124*, 073602. [CrossRef]
35. Shen, L.-T.; Tang, C.-Q.; Shi, Z.; Wu, H.; Yang, Z.-B.; Zheng, S.-B. Squeezed-Light-Induced Quantum Phase Transition in the Jaynes–Cummings Model. *Phys. Rev. A* **2022**, *106*, 023705. [CrossRef]
36. Lü, J.-H.; Ning, W.; Zhu, X.; Wu, F.; Shen, L.-T.; Yang, Z.-B.; Zheng, S.-B. Critical Quantum Sensing Based on the Jaynes–Cummings Model with a Squeezing Drive. *Phys. Rev. A* **2022**, *106*, 062616. [CrossRef]
37. Zhu, G.L.; Hu, C.S.; Wang, H.; Qin, W.; Lü, X.Y.; Nori, F. Nonreciprocal Superradiant Phase Transitions and Multicriticality in a Cavity QED System. *Phys. Rev. Lett.* **2024**, *132*, 193602. [CrossRef]
38. Song, H.; Zhu, G.L.; Wang, X. Dissipative superradiant phase transitions and multicriticality induced by two-mode squeezing. *Phys. Rev. A* **2025**, *112*, 023704. [CrossRef]
39. Scully, M.O.; Zubairy, M.S. *Quantum Optics*; Cambridge University Press: Cambridge, UK, 1999.
40. Agarwal, G.S. *Quantum Optics*; Cambridge University Press: Cambridge, UK, 2012.
41. Lü, X.Y.; Wu, Y.; Johansson, J.R.; Jing, H.; Zhang, J.; Nori, F. Squeezed Optomechanics with Phase-Matched Amplification and Dissipation. *Phys. Rev. Lett.* **2015**, *114*, 093602. [CrossRef]
42. Qin, W.; Kockum, A.F.; Muñoz, C.S.; Miranowicz, A.; Nori, F. Quantum amplification and simulation of strong and ultrastrong coupling of light and matter. *Phys. Rep.* **2024**, *1078*, 1–59. [CrossRef]
43. Gardiner, C.W.; Collett, M.J. Input and Output in Damped Quantum Systems: Quantum Stochastic Differential Equations and the Master Equation. *Phys. Rev. A* **1985**, *31*, 3761–3774. [CrossRef]
44. Baumann, K.; Guerlin, C.; Brennecke, F.; Esslinger, T. Dicke Quantum Phase Transition with a Superfluid Gas in an Optical Cavity. *Nature* **2010**, *464*, 1301–1306. [CrossRef]
45. Bina, M.; Amelio, I.; Paris, M.G.A. Dicke Coupling by Feasible Local Measurements at the Superradiant Quantum Phase Transition. *Phys. Rev. E* **2016**, *93*, 052118. [CrossRef]

Disclaimer/Publisher's Note: The statements, opinions and data contained in all publications are solely those of the individual author(s) and contributor(s) and not of MDPI and/or the editor(s). MDPI and/or the editor(s) disclaim responsibility for any injury to people or property resulting from any ideas, methods, instructions or products referred to in the content.